

Article

Structural Chemistry of Akdalaite, $\text{Al}_{10}\text{O}_{14}(\text{OH})_2$, the Isostructural Aluminum Analogue of Ferrihydrite

John B. Parise^{1,2,3,*} , Bingying Xia⁴, Jack W. Simonson⁴, William R. Woerner⁵, Anna M. Plonka⁶ , Brian L. Phillips¹ and Lars Ehm^{1,7}

¹ Department of Geosciences, Stony Brook University, Stony Brook, NY 11794, USA; Brian.phillips@stonybrook.edu (B.L.P.); Lars.Ehm@stonybrook.edu (L.E.)

² Department of Chemistry, Stony Brook University, Stony Brook, NY 11794, USA

³ Joint Photon Sciences Institute, Stony Brook University, Stony Brook, NY 11794, USA

⁴ Department of Physics, Farmingdale State College, Farmingdale, NY 11735, USA; xiab@farmingdale.edu (B.X.); simonsjw@farmingdale.edu (J.W.S.)

⁵ EAG Laboratories, 625-B, Alfred Nobel Dr, Hercules, CA 94547, USA; william.woerner@gmail.com

⁶ Department of Materials Science and Chemical Engineering, Stony Brook University, Stony Brook, NY 11794, USA; Anna.Plonka@stonybrook.edu

⁷ Mineral Physics Institute, Stony Brook University, Stony Brook, NY 11794, USA

* Correspondence: john.parise@stonybrook.edu

Received: 21 April 2019; Accepted: 9 May 2019; Published: 12 May 2019



Abstract: As part of an effort to characterize clusters and intermediate phases likely to be encountered along solution reaction pathways that produce iron and aluminum oxide-hydroxides from Fe and Al precursors, the complete structure of $\text{Al}_{10}\text{O}_{14}(\text{OH})_2$ (akdalaite) was determined from a combination of single-crystal X-ray diffraction (SC-XRD) data collected at 100 K to define the Al and O positions, and solid-state nuclear magnetic resonance (NMR) and neutron powder diffraction (NPD) data collected at room temperature (~300 K) to precisely determine the nature of hydrogen in the structure. Two different synthesis routes produced different crystal morphologies. Using an aluminum oxyhydroxide floc made from mixing AlCl_3 and 0.48 M NaOH, the product had uniform needle morphology, while using nanocrystalline boehmite (Vista Chemical Company Catapal D alumina) as the starting material produced hexagonal plates. Akdalaite crystallizes in the space group $\text{P}6_3mc$ with lattice parameters of $a = 5.6244(3)$ Å and $c = 8.8417(3)$ Å (SC-XRD) and $a = 5.57610(2)$ Å and $c = 8.77247(6)$ Å (NPD). The crystal structure features $\text{Al}_{13}\text{O}_{40}$ Keggin clusters. The structural chemistry of akdalaite is nonideal but broadly conforms to that of ferrihydrite, the nanomineral with which it is isostructural.

Keywords: akdalaite; ferrihydrite; solution synthesis; X-ray diffraction; NMR spectroscopy; bond valence sums

1. Introduction

Nanocrystalline materials are ubiquitous in modern materials science and technology [1]. They are also prevalent throughout the natural environment, where they commonly act as substrates for the sorption, transport, and desorption of contaminants [2,3]. Increasingly, anthropogenic-generated nanoparticles [4,5] are recognized as posing an ecotoxicological risk. Nanoscale oxides and oxide-hydroxides produced via metal hydrolysis routes in solution, such as those of iron and aluminum, possess unique surface properties utilized for catalysis, separations, and other important applications [6–8]. Solution synthesis in general promotes reactions at lower T, where weak solvent–solute interactions and changes in surface energies contribute sufficiently to the overall energy of the system. Small changes in synthesis conditions radically alter the properties of the materials produced.

Unlike simpler traditional cook-and-look synthesis studies, we seek to directly interrogate the changes occurring along a solution reaction pathway leading to the formation of nanoparticles (NPs) and nanocrystals (NCs) using combinations of in situ experimentation and computational tools to build structure models of intermediate species and products. This requires an exquisite knowledge of the phases likely to be encountered along the solution synthesis pathway. Especially in the early stages of synthesis, clusters and nanocrystalline materials dominate, and so local structure probes such as solution nuclear magnetic resonance (NMR) spectroscopy and pair distribution function (PDF) analysis [9–11] are needed to fully characterize the atomic arrangements. It is also useful to benchmark resonant (NMR, X-ray absorption spectroscopy) and nonresonant (scattering) techniques against one another in order to obtain an appreciation of each technique's advantages and disadvantages. For example, solution NMR spectroscopy excels at the characterization of mixtures of soluble species, clusters, and small (<2 nm) particles in solution [12], while PDF excels at characterizing NPs and, perhaps, small clusters during the early stages of synthesis [13,14]. If structure models for possible species in solution are known, the sensitivity of PDF to mixtures of dilute species is also testable.

The Al- and Fe-oxide-hydroxides are good systems in which to test the relative sensitivity of NMR and PDF since there are many isomorphous compounds. Synthesis of Fe- and Al-oxyhydroxides involve ololation reactions [12,14–16]—condensation of soluble precursors to form isostructural and Al/Fe substitutional phases. Multimeric species ($[M_{13}O_4(OH)_{24}(H_2O)_{12}]^{7+}$, M = Al, Fe) are implicated in pathways from soluble ions to oxide-hydroxides. Total X-ray scattering studies [9,10] show that the structure of the ubiquitous ferrihydrite phase contains motifs of Fe₁₃ Keggin clusters, which are implicated in the growth of ferrihydrite [16]. This tantalizing evidence that Fe and Al systems form similar prenucleation clusters, and so share complementary points of leverage along the reaction pathway, suggests that joint NMR and PDF studies of the ololation reactions involving Al will be useful to understand the phase evolution of Fe pathways as well. Before carrying out in situ studies, it is important that at least phases described previously in the Al- and Fe-oxide-hydroxide systems be well characterized, structurally and chemically. It is with this wider goal in mind that we undertook a comprehensive study of the structure related to the clusters and some products encountered in both Fe- and Al-O-OH systems: akdalaite.

An accurate structure for akdalaite will also help address controversies about the structural chemistry of ferrihydrite. The structure of ferrihydrite, the Fe analogue of akdalaite, was the focus of scientific debate for at least half a century, and much of the literature for that period is summarized in a review by Jambor and Dutrizac [17]. Following publication of a multiphase model, [18] a single-phase model for the atomic arrangements in ferrihydrite emerged based on the structure of akdalaite, as it provided the best match to the X-ray PDF patterns for all ferrihydrite particle sizes. The akdalaite model for ferrihydrite first presented by Michel et al. (2007) [10] and later refined by Michel et al. [9] was immediately controversial, with objections dealing with unusual crystal chemistry, partially occupied metal sites, and refinement strategies [19–22]. Isostructural akdalaite, synthesized here as both powder and single-crystal forms, has a well-defined structure and can be subjected to rigorous unit-cell-based crystallographic analysis to address the problems outlined below.

There are aspects of the akdalaite-based model for ferrihydrite, ideally Fe₁₀O₁₄(OH)₂, which are inconsistent with expectations based on accepted crystal chemical arguments; but are these deviations from the expected crystal chemistry intrinsic to the model shared by both akdalaite and ferrihydrite? In the “Michel model” (MM) for ferrihydrite, some bond valence sums are inconsistent with the expected values of +3 and −2 for Fe³⁺, O^{2−}, and OH[−] (Figure 1). Additionally, in the MM, certain Fe–Fe distances and Fe-centered octahedral distortions are anomalous compared with values expected based on the crystal chemistry of the iron oxides and hydroxides [20,21]. The degree of site disorder in ferrihydrite also appears to be synthesis path dependent, with additives and aging protocols [9,10] producing a larger particle size with few defects and pronounced ferrimagnetism relative to more disordered ferrihydrite precursors. It appears isostructural akdalaite crystallizes as stoichiometric Al₁₀O₁₄(OH)₂, possessing, as confirmed in our study detailed below, a defect-free structure. To evaluate

the validity of crystal chemical arguments, and to provide a base-line structure to which various path-dependent ferrihydrite preparations can be compared, the complete akdalaite model, including a detailed description of the nature of the hydrogen environment, is presented here in detail.

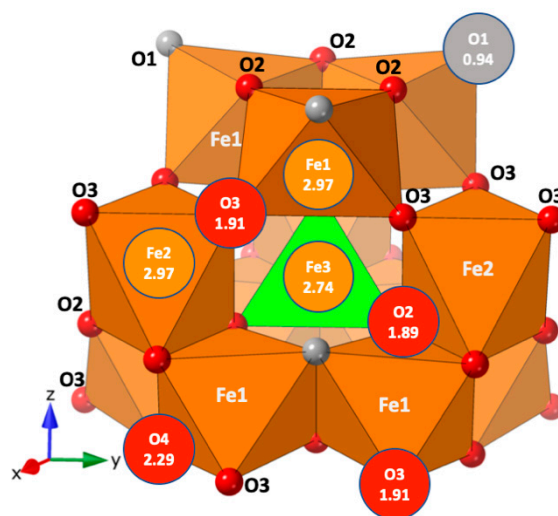


Figure 1. The revised polyhedral structure model of ferrihydrite from Michel et al. (2010) [9] shown in the Keggin motif with the calculated bond valences of each site. The Fe octahedra are brown, the tetrahedral Fe is green, and the Fe sites would ideally have bond valence sums (BVS) of 3; oxygen atoms are red, hydroxyl (O1) is gray, and they would ideally have BVS of 2 and 1, respectively.

2. Materials and Methods

2.1. Sample Preparation and Provenance

Samples of crystalline akdalaite were synthesized hydrothermally in cold-seal pressure vessels [23] using a modified method of Rosenberg (2006) [24]. The starting materials were sealed in a gold capsule (2 cm long, 5-mm diameter) with an aqueous solution of 0.54 M NH_4F in a 2:1 weight ratio. The capsule was subjected to 2 kbar and 475 °C in the cold-seal vessel for 5 days. Two different starting materials were used, and they produced different crystal morphologies. When the starting material was a synthetic aluminum oxyhydroxide floc (Al-floc) [25], the akdalaite product had uniform needle morphology and was typically 50 μm long with an aspect ratio of about 20 (see Supplementary Materials, Figure S1). The synthetic Al-floc material was formed by the instantaneous mixing of 0.2 M AlCl_3 and 0.48 M NaOH in equal volumes. The Al-floc gel was then centrifuged, decanted, and dried at 50 °C for 12 h. This was chosen as a starting material as it is amorphous and thought to be composed mostly of aggregates of Al_{13} Keggin polyoxocations with Al in 4, 5, and 6 coordination, which would act as nucleation sites and allow for the rapid transformation to akdalaite [25].

Larger akdalaite crystals of a size suitable for single-crystal X-ray diffraction (SC-XRD) were synthesized using nanocrystalline boehmite (Vista Chemical Company Catapal D alumina) as the starting material (Figure S2). The akdalaite crystals produced from boehmite had a hexagonal plate morphology with a diameter of $\sim 20 \mu\text{m}$, which were large enough for synchrotron single-crystal diffraction studies. After hydrothermal synthesis, sample powders were washed repeatedly with DI water to remove any possible remnants of recrystallized NH_4F and dried at 50 °C for 12 h. In order to produce enough sample for powder neutron diffraction, a single synthesis experiment was conducted using nanocrystalline boehmite and a 5.5-cm-long gold capsule.

2.2. Analytical Methods

Bulk sample identification and phase purity were initially checked using laboratory PXRD. The data were collected using a Rigaku Ultima IV (Cu $K\alpha$ radiation) with a D/TeX linear position

sensitive detector. Patterns were collected over a range of $5^\circ \leq 2\theta \leq 90^\circ$ with a step size of 0.01° at a rate of $1^\circ/\text{min}$. SEM images of akdalaite synthesized using synthetic Al-floc starting material were obtained using a LEO 1550 scanning electron microscope at an operating voltage of 20 kV. The images of akdalaite synthesized from boehmite were obtained with a Hitachi S-2600N at an operating voltage of 10 kV. Samples were mounted on aluminum sample holders with carbon tape and gold coated using an EMS-550X sputter coater.

X-ray diffraction data for a single crystal of synthetic akdalaite (hexagonal plate morphology) were collected at 100 K using a three-circle Bruker D8 diffractometer equipped with an APEXII detector ($\lambda = 0.41328 \text{ \AA}$) using $0.5^\circ \varphi$ scans at the ChemMatCars beamline (sector 15) of the Advanced Photon Source (APS).

Neutron powder diffraction (NPD) data were collected to better resolve the position of hydrogen and generate a complete akdalaite structure model. Time of flight (TOF) NPD data were collected using the POWGEN instrument (BL-11) at the Spallation Neutron Source of Oak Ridge National Laboratory. Approximately 1 g of powdered sample was loaded into a 6-mm vanadium can for measurements at room temperature (299 K). POWGEN data were collected for 3 h using frame 2 ($0.35 \text{ \AA} \leq d \leq 3.0 \text{ \AA}$). Since akdalaite has about 8 mol % structural hydrogen, the contribution of incoherent neutron scattering contribution was judged to be sufficiently small, and so as-synthesized hydrogenous akdalaite was used.

All solid-state NMR spectra were acquired with a 500 MHz (11.7 T) Varian Infinity-Plus spectrometer equipped with Varian/Chemagnetics sample probe assemblies configured for 3.2- and 4.0-mm (o.d.) rotors and operating at 130.3 and 499.78 MHz for ^{27}Al and ^1H , respectively. The ^{27}Al magic angle spinning (MAS) NMR spectra were acquired at a spinning rate of 20 kHz with 0.5- μs pulses ($\nu_{\text{RF}} = 50 \text{ kHz}$) and 0.5-s relaxation delay. Over 96% of the magnetization was recovered under these conditions. No differential relaxation effects were noted in spectra taken with relaxation delays that varied from 60 to 0.5 s. The ^{27}Al multiple-quantum MAS data (MQ/MAS) were taken at a 20-kHz spinning rate using 1.9- μs excitation and 0.8- μs conversion pulses ($\nu_{\text{RF}} = 132 \text{ kHz}$), followed by an 18- μs selective 90° zero-quantum filter pulse, with phase cycling to select the triple quantum coherence. We collected 80 hypercomplex points with a t_1 increment of 25 μs , each the sum of 384 acquisitions taken with a 0.5-s relaxation delay. The ^1H MAS/NMR spectrum was obtained at a spinning rate of 15 kHz using 1- μs pulses ($90^\circ = 4 \mu\text{s}$) and a 4-s relaxation delay. Chemical shifts are reported relative to a 0.1 *m* aqueous AlCl_3 solution for ^{27}Al and tetramethylsilane (TMS) for ^1H .

3. Results

Laboratory powder XRD and SEM investigations indicated akdalaite synthesized using the Al-floc starting material was nearly pure, with minor corundum impurity (Supplementary Materials Figure S1). The akdalaite synthesized from nanocrystalline boehmite also had a minor corundum impurity but had a hexagonal plate morphology suitable for SC-XRD (Supplementary Materials Figure S2). The 1-g sample synthesized from boehmite for NPD utilized a much longer capsule (5.5 cm) and was likely subject to a higher thermal gradient in the cold-seal vessel, which resulted in a higher amount of impurity corundum (Supplementary Materials Figure S3).

3.1. Single-Crystal X-ray Diffraction

A single crystal of akdalaite with hexagonal plate morphology was selected from the samples prepared from boehmite (Supplementary Materials Figure S2). The summary of akdalaite crystallographic data, SC-XRD structural refinement details, refined parameters, and other structural details are provided in Tables A1–A5 in the Appendix A. After reducing the SC-XRD data [26], the crystal structure was solved using a charge flipping algorithm [27,28], and inspection of the Wilson plot and the intensity weighted reciprocal lattice, including Bijovet pairs, suggested the structure was acentric with a point group of 6 *mm* [29]. We note that the charge flipping algorithm only satisfactorily converged in the noncentrosymmetric space group $P6_3mc$. Ab initio structure determination followed by least-squares

Fourier cycling confirmed the accepted space group assignment and located the nonhydrogen atoms. Displacement parameters for all the nonhydrogen atoms were refined anisotropically. The hydrogen atom was located from a Fourier difference map and geometrically constrained. The refinement using SC-XRD data confirmed the proposed structure of “tohdite” [30] and found residual electron density from hydrogen around site O1. The weak X-ray scattering from hydrogen did not allow a full refinement but did provide an adequate starting site position for NPD Rietveld refinements described below. Because the positions of hydrogen, critical for the determination of site bond valence sums, are better determined from the NPD data, we discuss the structural details with reference to the neutron refinement and make reference to the SC-XRD results where they fortify or modify the conclusions derived from the NPD data.

3.2. Neutron Powder Diffraction

Inspection of the NPD patterns (Figure 2) indicated it could be indexed on the basis of the unit cell and Laue symmetry determined from SC-XRD data. The GSAS/EXPGUI Rietveld software package [31,32] was used to refine this model. A subsequent anisotropic refinement of the H site displacement parameters revealed a distribution of nuclear density smeared in a disk shape perpendicular to the threefold axis, indicating the H atoms deviate from the ideal $2a$ ($3m$) site symmetry. This is suggestive of the type of H site disorder previously described in $M(OH)_2$ hydroxides such as $Mg(OH)_2$ (brucite [33]), where the H site is modeled as a threefold split site with $1/3$ site occupancy [33,34]; this involves moving the H site from the threefold axis, at site $2a$ ($0,0,z$), to site $6c$ ($2x,x,1/2+z$) with site symmetry $\cdot m$ in space group $P6_3mc$ (No. 186). The refinement details, refinement statistics, refined parameters, interatomic distances, and angles are presented in Appendix B in Tables A6–A10. The split-site refinement suggests the H atoms deviate from the axis due to hydrogen bonding with the O3 site. The structure of the akdalaite model with the split hydrogen site is detailed in Figure A1.

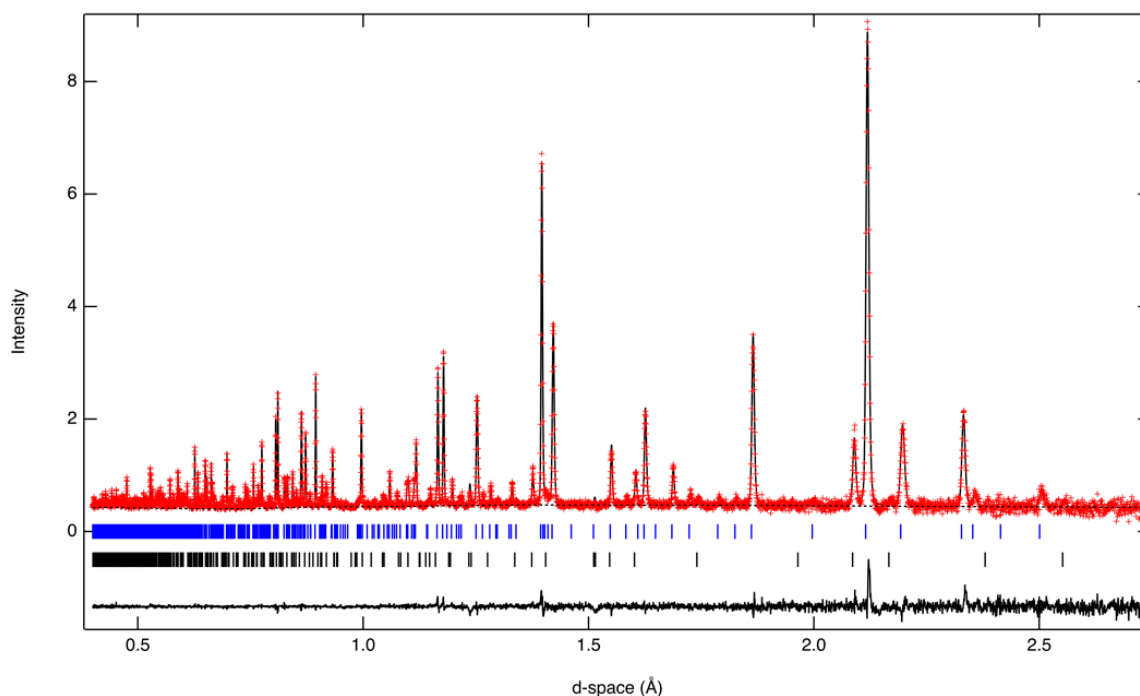


Figure 2. Fit to neutron data for $Al_{10}O_{14}(OH)_2$; observed and calculated data are red crosses and the continuous black line, respectively. The dotted blue and solid black curves represent the background and the difference between observed and calculated data, respectively. The vertical blue and black lines mark the positions of Bragg reflections from the $Al_{10}O_{14}(OH)_2$ (akdalaite) and Al_2O_3 (corundum), respectively.

3.3. Solid State NMR

Solid-state NMR data gave additional insight into the local environments of Al and H in akdalaite and confirmed the akdalaite structure solved from SC-XRD and further refined from NPD. The ^{27}Al MAS NMR spectra of synthetic and natural akdalaite (Figure S4) indicate both samples have six- and four-coordinate Al.

The synthetic sample was further studied with ^{27}Al MQ/MAS to determine the number and proportion of distinct Al sites in akdalaite. The spectra from the ^{27}Al MQ/MAS study revealed three distinct Al sites—two octahedral and one tetrahedral (Figure 4)—with isotropic peaks at 11.5, 23.4, and 77.5 ppm in F1 (vertical axis in Figure 3). Simulation of the separate F2 cross sections to second-order quadrupolar peak shapes (Figure 3, right panel) yielded the chemical shift (δ_{iso}), quadrupolar coupling constant (Cq), and asymmetry parameter (η) for each resolved site, compiled in Table 1. These values were then used to fit the quantitative MAS spectrum to a sum of second-order quadrupolar center bands, yielding an Al site distribution of $59\% \pm 2\%$ for the Al1 octahedral site, $22\% \pm 2\%$ for the Al2 octahedral site, and $20\% \pm 2\%$ for the Al3 tetrahedral site, in reasonable agreement with the X-ray- and neutron-derived models.

Table 1. ^{27}Al nuclear magnetic resonance (NMR) parameters for synthetic akdalaite, obtained from simulation of the F2 cross sections of the ^{27}Al multiple-quantum magic angle spinning (MQ/MAS) NMR spectrum (Figure 3). Estimated uncertainties are ± 0.2 ppm for the isotropic chemical shift (δ_{iso}), ± 0.1 MHz for the quadrupolar coupling constant (Cq), and ± 0.1 for the asymmetry parameter (η). $\delta_{\text{F1,obs}}$ is the observed peak position in the MQ/MAS F1 dimension (vertical spectrum in Figure 3), whereas $\delta_{\text{F1,calc}}$ is calculated from the fitted quadrupolar coupling parameters.

Site	Type	δ_{iso} (ppm)	Cq (MHz)	η	$\delta_{\text{F1,calc}}$ (ppm)	$\delta_{\text{F1,obs}}$ (ppm)
Al1	octahedra	17.0	5.1	0.7	23.3	23.4
Al2	octahedra	10.3	2.3	0.2	11.4	11.5
Al3	tetrahedra	66.5	7.3 ₅	0	77.7	77.5

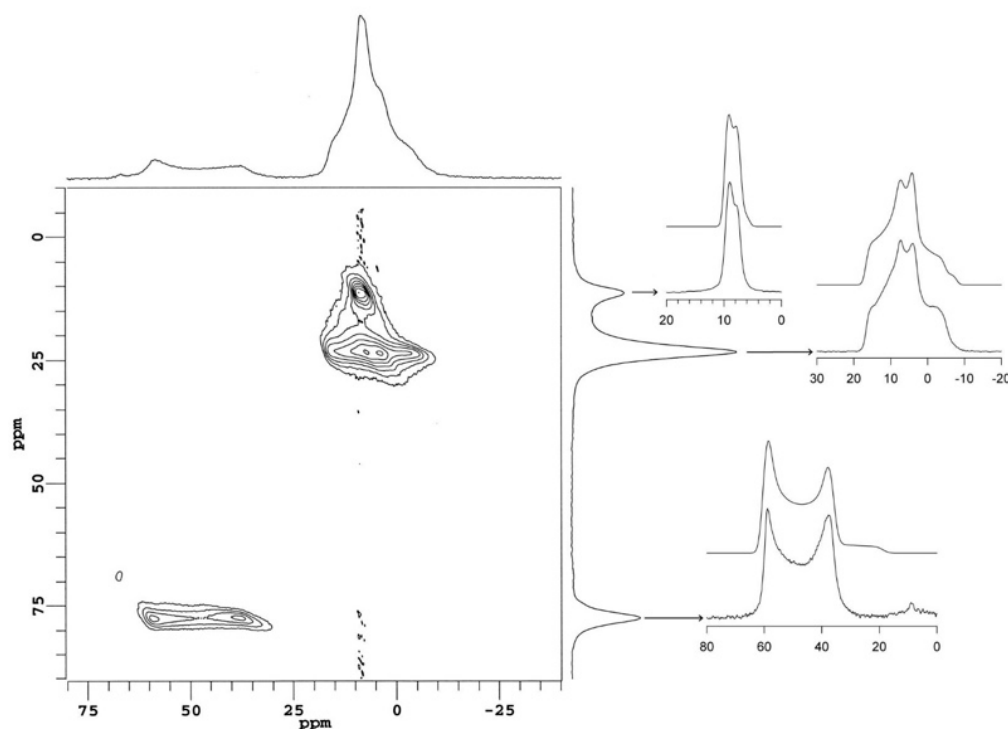


Figure 3. ^{27}Al MQ/MAS NMR spectrum of synthetic akdalaite. The top spectrum is the MAS dimension, while the right spectrum is the isotropic dimension. The individual site spectra are shown on the far right with the simulated spectra above the experimental.

The ^1H NMR spectrum consists primarily of a single, narrow central peak at +8.6 ppm, with two spinning sidebands, as shown in Figure 4. A small shoulder near +6.5 ppm (<5% intensity) likely arises from an impurity phase and/or surface adsorbed water. The single, well-resolved central peak indicates a single H site, and the small peak width (600 Hz) observed at this modest spinning rate (15 kHz) indicates a small homonuclear dipolar coupling characteristic of low hydrogen density [35,36]. In this chemical shift range, the literature data for ^1H indicate a good linear correlation with $d(\text{O} \dots \text{O})$ hydrogen bond lengths [35], although the relationship between chemical shift and hydrogen bond distance can also be expected to reflect other geometrical factors such as H–O distance and O–H \dots O angle. With that caveat, the observed shift at 8.6 ppm (Figure 4) is similar to that of diaspore ($\alpha\text{-AlOOH}$), which has a shift at +9.4 ppm and an O \dots O distance of ~ 2.65 Å [35] compared with an O \dots O distance of ~ 2.91 Å in akdalaite.

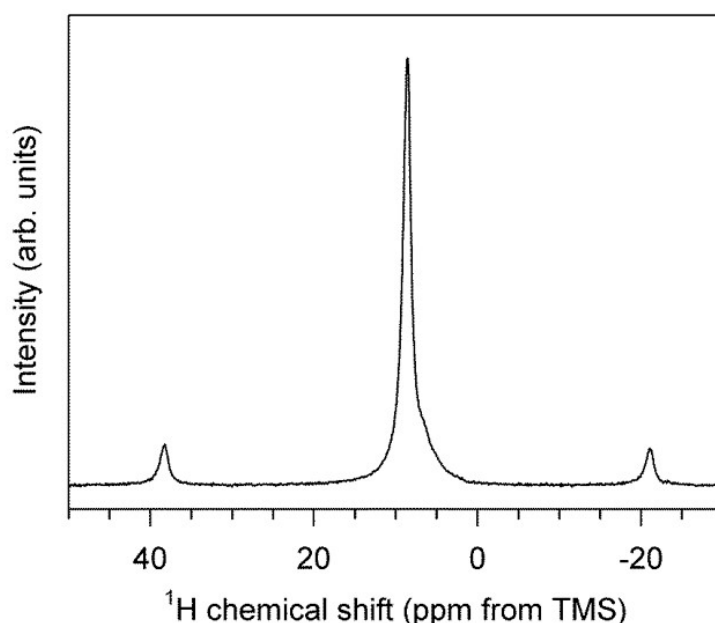


Figure 4. ^1H MAS NMR spectra of synthetic akdalaite. The central peak has a chemical shift of +8.6 ppm. Spinning side bands shown outside central peak.

3.4. Crystal Chemical Analysis

The results from SC-XRD, NPD, and NMR were used to form a complete structural model of akdalaite (Figures 5 and 6) for comparison with ferrihydrite [9]. The bond valence sums (BVS) were calculated from the NPD data in the same manner as ferrihydrite, where the total site valence (V_i) is the sum of valences (S_{ij}) associated with the bond between atoms i and j [37–39]. The individual bond valences were calculated using Equation (1) with the experimentally determined bond lengths (R_{ij}) and the empirical constants R_0 and b determined from valence analysis of known compounds. For Al–O bonds, $R_0 = 1.651$ and $b = 0.37$ [19,37].

$$V_i = \sum_j S_{ij} = e^{(R_0 - R_{ij})/b} \quad (1)$$

The interatomic distances and bond valence sum listed in Tables A8 and A9, and overlaid on the structure in Figures 5 and 6, broadly conform to values expected from the isostructural MM model of ferrihydrite [9]. The contribution of hydrogen to the oxygen bond valence was accomplished using different empirical constants for the shorter donor O–H and longer acceptor O \dots H bonds (Table A8). Previous studies found that hydrogen bonding is unlike typical cation–anion interactions and the hydrogen bonding interactions have to be treated differently [38–40]. The aluminum sites show signs of over- and underbonding as the BVS of the tetrahedral site (Al3) is underbonded at 2.71 Å, below

the ideal value of 3 for aluminum (Figure 6) but conforming to the result reported for the MM model (Figure 1). The octahedral aluminum sites of Al1 and Al2 are closer to ideal being, 3.11 and 2.79 Å, respectively. This is similar to Fe BVS of the ferrihydrite model (Figure 1), where the octahedral sites are 2.97 while the tetrahedral site is underbonded at 2.74.

The oxygen BVS sums are also similar to those found in ferrihydrite, with the O4 site overbonded at 2.15 and 2.29 in akdalaite (Figure 6) and ferrihydrite (Figure 1), respectively. The hydroxyl oxygen (O1) has an understandably low BVS at 1.44 prior to accounting for hydrogen bonding. After accounting for hydrogen bonding, the oxygen sites are slightly over- and underbonded (Tables A4 and A9). The akdalaite model, especially that derived from the neutron data, correctly takes account of the H contribution to the BVS for oxygen. In the case of ferrihydrite, the oxygen BVS is estimated. With this caveat, the akdalaite and ferrihydrite BVS are quite comparable, further suggesting deviations from ideality are inherent to bond strain associated with the structure type.

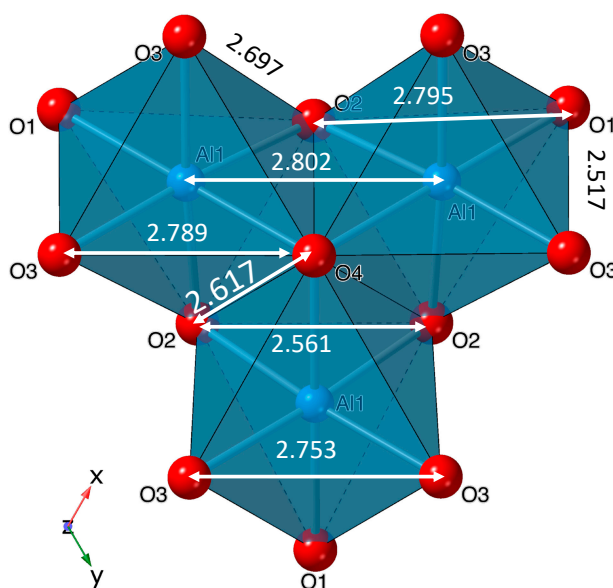


Figure 5. Selected interatomic distances in the Al1-trimer in akdalaite.

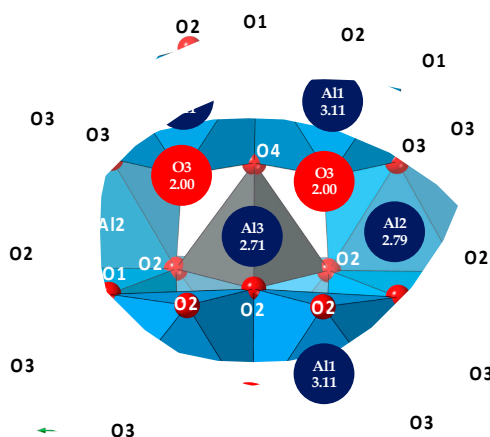


Figure 6. Structure of akdalaite refined from neutron powder diffraction (NPD) data shown in the δ -Keggin motif with the calculated bond valence sums of each site prior to adding contributions from hydrogen. The Al octahedra are blue, the tetrahedral Al is gray, and oxygen atoms are red.

In addition, for any nonideality in bond valence sum, some of the Al bonding environments in akdalaite have characteristics that are similar to those observed in the ferrihydrite model. In analyzing the Al–Al distances (Table A10, Figure 5), it is clear they are nonideal. The Al1–Al1 bond distance

between the edge sharing octahedra is 2.802 Å, much shorter than the other edge sharing octahedra where the Al1–Al2 distance is 3.018 Å (Table A10). The short edge sharing distance between Al1–Al1 is close to that of the Al octahedral face sharing distance of corundum at 2.654 Å and is ~9% shorter than the other edge sharing Al1–Al2 distance, 3.339 Å (Table A4, Figure 5). In ferrihydrite, the Fe1–Fe1 bond distance is 2.907 Å, which is ~11% shorter than the other shared edge Fe1–Fe2 bond distance of 3.261 Å, much like the Al sites in akdalaite. However, this Fe1–Fe1 edge sharing distance is only slightly larger than the Fe octahedra face sharing distance in hematite (2.895 Å) [20,41].

The Al2 octahedra in akdalaite are also distorted in that the Al is off center so much that three of the Al2–O distances are only 1.874(3) Å, which are close to the Al–O bond distances in the Al3-centered tetrahedron, between 1.788(1) and 1.818(4) Å (Figure 5, Table A8). The ferrihydrite Fe2 octahedral distortion also results in uncharacteristically short Fe–O distances of 1.881 Å, which in turn are shorter than some of the tetrahedral Fe–O distances (1.931 Å). The atypical bonding at the Al2 site observed in akdalaite is also present at the Fe2 site in the ferrihydrite model, again suggesting considerably strained structures, to the point of violating accepted principles [21].

Thorough crystal chemical analysis has revealed that most of the anomalous aspects of the ferrihydrite model are intrinsic to the akdalaite structure. The only structural oddity of the MM ferrihydrite model [9] not observed in the akdalaite structure, and for which the MM model was criticized, is the distorted edge sharing O–O bonding distances between the Fe1 sites where the shared edge was longer than the unshared edge (Figure 1). The Al1 octahedra have a slightly shorter O–O distance on the shared edge (2.617 Å) in comparison with the unshared edge (2.697 Å) in accordance with Pauling’s distortion rule [42]. Otherwise, the anomalous crystal chemical trends that are observed in akdalaite are present in the ferrihydrite model. These differences have been discussed previously as possibly arising from the assumptions inherent in the fitting of PDF data from which the MM model is derived.

It was emphasized in the original single-phase ferrihydrite model refinement that while the structure can be described by an idealized periodic model, real-space fitting does not take into account that “second-order effects such as disorder, surface relaxation, internal strain, defects (e.g., stacking faults), particle shape, and/or interparticle correlations may also contribute to the experimental PDFs” [10]. The PDF patterns of nanoparticles are heavily influenced by the size and morphology of the particles, as this will weight some pair correlations more than others [43–45]. Treatment of the nanocrystal morphology, such as modeling the ferrihydrite plate morphology as a sphere, can result in model distortions in order to better fit the data.

Further, as the nanoparticles of ferrihydrite have a high surface area, surface interaction and relaxation will also have a significant impact on the total scattering. In crystals and crystallites, the surface-area-to-volume ratio is so small that surface structure will have a negligible contribution to the scattering. However, in the case of nanoparticles such as ferrihydrite, the surface comprises a significant portion of the structure and surface contribution to the total scattering is no longer minor. A study of ferrihydrite surface structure elucidated that the Fe sites exposed at the surface are dominantly the Fe1 octahedra [46]. The shorter-than-expected Fe1–Fe1 distance and distortion of the Fe1 octahedra is likely due to the strains placed on the sites at the surface of ferrihydrite particles. Thus, surface interactions and relaxation will preferentially distort the Fe1 octahedra and the distortions on the surface will have a significant contribution to the total scattering and PDF. Thus, when a unit cell approach to modeling the total scattering and PDF is used, the bulk Fe1 site will appear distorted due to the contributions of distorted Fe1 octahedra at the surface—the bulk and surface Fe1 sites are average in such an approach. While the previous critiques of the ferrihydrite crystal chemistry were originally valid, crystal chemical analysis has shown that these are inherent characteristics of the akdalaite model, and exacerbated distortions likely arise from the nonideal treatment of PDF data during model refinement. It is for this reason that the fully ordered structure of akdalaite is an important benchmark for the isostructural bulk structure of ferrihydrite and an excellent starting point for calculations of the distortions resulting from disorder, partial site occupancy, and surface relaxation. Further validation of the appropriateness

of the akdalaite model as a proxy for the calculation of possible ferrihydrite disordered structures is provided in the Supplementary Materials.

4. Conclusions

Through the combined study of akdalaite with SC-XRD, NPD, and NMR, a complete structural model of akdalaite has been created, and this can be used as a basis for the calculation of ordered and disordered nanoparticle ferrihydrite, its isostructural Fe analogue. The positions for hydrogen, critical for reliable calculation of the BVS, are distributed over a split site about the threefold axis with $1/3$ occupancy. Crystal chemical analysis revealed abnormal bond valences with over- and underbonding of atoms within the structure as well as unexpectedly close O . . . O distances on Al-octahedral edge sharing at the Al1 site and distortions at the Al2 site. This mirrors crystal chemical anomalies for the oft-criticized single-phase ferrihydrite model and suggests that these anomalies are inherent to the structure shared by both akdalaite and ferrihydrite. Further study with X-ray total scattering provided additional evidence that the akdalaite structure model is appropriate for ferrihydrite. The exacerbation of the akdalaite crystal chemical oddities in the ferrihydrite model is not due to inappropriate use of the model but rather how the model is treated in modeling the PDF patterns.

Supplementary Materials: The COD entries 3000229 and 3000230 contain the supplementary crystallographic data for the single-crystal X-ray and neutron powder refinements, respectively, referenced in this paper. These data can be obtained free of charge via <http://www.crystallography.net/cod/search.html>. The following are available online at <http://www.mdpi.com/2073-4352/9/5/246/s1>, Figure S1: The PXRD pattern (top) and SEM image (bottom) of akdalaite synthesized from Al-floc showing only a minor impurity of corundum (red tick), Figure S2: The PXRD pattern (top) and SEM image (bottom) of akdalaite synthesized from boehmite in a 2-cm-long capsule showing only a minor impurity of corundum (red tick), Figure S3: The XRD pattern of akdalaite synthesized from boehmite in a 5.5-cm-long capsule showing corundum (red tick) present as a minor phase, Figure S4: ^{27}Al MAS NMR spectra of synthetic crystalline akdalaite and natural akdalaite, Figure S5: Calculated pair distribution functions (PDFs) of hematite and corundum, Figure S6: Plot of the r-shift of identical peaks in the calculated PDFs of hematite and corundum, Figure S7: Calculated PDFs of hematite and corundum after the corundum data have been shifted to account for the different M–O differences with the fitted linear r-shift equation (Equation (2)), Figure S8: (top) Comparison of X-ray PDF data from crystalline akdalaite and 6-line ferrihydrite. (middle) X-ray PDF data from 6-line ferrihydrite and r-shifted akdalaite which has been adjusted to have approximately equivalent M–O distances as those of Fe–O. (bottom) Same shifted data as middle but the akdalaite data has had a spherical envelope function applied so intensities are representative of a 3-nm spherical particle.

Author Contributions: J.B.P., B.L.P., W.R.W., L.E., and A.M.P. conceived and designed the experiments together; W.R.W., B.L.P., and A.M.P. performed the experiments; J.B.P., B.X., J.W.S., and W.R.W. analyzed the data; J.B.P. wrote and submitted the paper.

Acknowledgments: This work was supported as part of GENESIS: A Next Generation Synthesis Center, an Energy Frontier Research Center funded by the U.S. Department of Energy, Office of Science, Basic Energy Sciences under Award Number DE-SC0019212. A portion of this research used resources at the POWGEN beamline at the Spallation Neutron Source, a Department of Energy (DOE) Office of Science User Facility operated by the Oak Ridge National Laboratory (ORNL), managed by UT Battelle, LLC for the U.S. DOE under contract DE-AC05-00OR22725. This research also used resources of the ChemMatCARS beamline (supported by the Divisions of Chemistry (CHE) and Materials Research (DMR), National Science Foundation, under grant number NSF/CHE- 1834750) at sector 15 of the Advanced Photon Source, a U.S. DOE Office of Science User Facility operated for the DOE Office of Science by Argonne National Laboratory under Contract No. DE-AC02-06CH11357. The authors wish to thank scientists and technicians working at these institutions for their help and scientific advice for this research. Travel to the SNS and APS and support for the hydrothermal syntheses were provided by Stony Brook University through its Joint Photon Sciences Institute. We are especially grateful to Alwin James for help with COD submissions.

Conflicts of Interest: The authors declare no conflict of interests.

Appendix A.

Results of Single-Crystal X-ray Diffraction Refinement

Refinement parameters and results derived from the SC-XRD data are summarized in Tables A1–A3, while selected interatomic distances and angles as well as bond valence sums are summarized in

Tables A4 and A5. The overall structure is depicted as a polyhedral model in Figure 1. The nature of the hydrogen bonding is depicted in Figure A1.

Table A1. Crystal data and structure refinement parameters for single-crystal X-ray diffraction (SC-XRD).

Parameter	Value
Sample	akdalaite
Empirical formula	Al ₅ HO ₈
Formula weight	263.9
Collection temperature (K)	100(2)
Wavelength (Å)	0.41328
Space group	P6 ₃ mc
a (Å)	5.56244(3)
b (Å)	5.56244(3)
c (Å)	8.8417(3)
Volume (Å ³)	242.22(2)
Z	2
Calculated density (g/cm ³)	3.6184
Absorption coefficient (mm ⁻¹)	0.265
F(000)	260.0
Crystal size (mm)	0.02 × 0.02 × 0.005
Θ range of data collection (°)	2.43–23.77
Index range	−10 ≤ h ≤ 10 −10 ≤ k ≤ 6 −16 ≤ l ≤ 17
Total reflections	5136
Independent reflections	712
R _{int}	0.047
Completeness to Θ _{max}	0.915
Goodness of fit	0.0233
Data/restraints/parameter	712/1/32
R ₁ (on F ₀ , I > 2σ(I))	0.0255
wR ₂ (on F ₀ ² , all data)	0.0621

Table A2. Akdalaite structure details from SC-XRD refinement.

Site	Wyckoff Pos.	x	y	z	U _{iso} (×10 ²) Å ²
Al1	6c	0.83432(3)	0.66864(6)	0.9775(4)	0.19
Al2	2b	1/3	2/3	0.7698(4)	0.16
Al3	2b	1/3	2/3	0.1604(4)	0.16
O1	2a	0	0	0.0971(4)	0.18
O2	6c	0.97188(14)	0.48594(7)	0.1129(4)	0.20
O3	6c	0.16594(9)	0.83406(9)	0.8739(4)	0.19
O4	2b	2/3	1/3	0.8667(4)	0.15
H1	2a	0	0	0.2062(5)	2.1(2)

Table A3. Refined akdalaite anisotropic displacement parameters from SC-XRD data (Å² × 10²).

Site	U ₁₁	U ₂₂	U ₃₃	U ₂₃	U ₁₃	U ₁₂
Al1	0.195(11)	0.160(13)	0.213(16)	0.080(6)	0.015(5)	0.030(10)
Al2	0.170(15)	0.170(15)	0.15(3)	0.0085(8)	0.0	0.0
Al3	0.154(15)	0.154(15)	0.18(3)	0.077(7)	0.0	0.0
O1	0.22(3)	0.22(3)	0.09(5)	0.110(14)	0.0	0.0
O2	0.17(2)	0.199(19)	0.22(3)	0.084(12)	−0.04(2)	−0.018(11)
O3	0.14(3)	0.14(3)	0.24(3)	0.03(3)	0.050(9)	−0.050(9)
O4	0.19(3)	0.19(3)	0.07(5)	0.095(17)	0.0	0.0
H1 *	U _{iso} = 2.1(2)					

* The H1 site was refined isotropically.

Table A4. Selected interatomic distances (Å) and angles (°) for akdalaite (Al₁₀O₁₄(OH)₂)—SC-XRD.

Al11	To	Dist.	$s_{ij}/\Sigma s_{ij}$ *	O2	O2	O3	O3	O4
	O1	1.930(3)	0.47	92.56(16)	92.56(16)	84.68(9)	84.68(9)	177.7(2)
	O2	1.971(3)	0.42	81.59(14)	90.17(9)	171.2(2)	85.71(10)	
	O2	1.971(3)	0.42	171.2(2)	90.17(9)	85.71(10)		
	O3	1.857(3)	0.57	97.88(16)	96.81(16)			
	O3	1.857(3)	0.57	96.81(16)				
	O4	1.905(3)	0.50					
BVS			2.965(9)					
Al1								
Al2	To	dist.		O2	O2	O3	O3	O3
	O2	2.033(4)	0.36	78.57(14)	78.57(14)	90.98(10)	166.4(2)	90.98(10)
	O2	2.033(4)	0.36	78.57(14)	90.98(10)	90.98(10)	166.4(2)	
	O2	2.033(4)	0.36	166.4(2)	90.98(10)	90.98(10)		
	O3	1.873(3)	0.55	97.90(16)	97.90(16)			
	O3	1.873(3)	0.55	97.90(15)				
	O3	1.873(3)	0.55					
BVS			2.720(9)					
Al2								
Al3	To	dist.		O2	O2	O4		
	O2	1.8100(14)	0.65	114.78(10)	114.79(11)	103.42(16)		
	O2	1.8100(15)	0.65	114.78(11)	103.42(16)			
	O2	1.8100(14)	0.65	103.42(16)				
	O4	1.824(5)	0.63					
BVS			2.561(10)					
Al3								
H1	To	Dist.		O3				
	O1	0.965(6)	0.66	132.53(11)				
	O3	2.194(4)	0.18					
BVS H1			1.189(4)					

* Bond valence $s_{ij} = \exp((R_0 - R_{ij})/B)$, where R_{ij} is the length of a bond between atoms i and j ; Σs_{ij} , the BVS around each atom should be equal to the valence (oxidation state) of that atom. For the values quoted, the parameters R_0 and B were taken from tabulations provided at the International Union of Crystallography: <https://www.iucr.org/resources/data/datasets/bond-valence-parameters> [39]. The R_0 and B parameters used were those compiled for Al³⁺ (1.651, 0.37) and H¹⁺ (0.569, 0.94) bonded to O²⁻.

Table A5. Akdalaite oxygen bond valence sums with hydrogen contribution—SC-XRD.

Site	BVS	Type
O1	2.071(8)	O-H
O2	1.852(6)	
O3	1.868(7)	O...H
O4	2.135(11)	

Appendix B.

Structural Description Using the Neutron Powder Diffraction Data

Refinement parameters and results derived from the NPD data are summarized in Tables A6 and A7. The overall structure is depicted as a polyhedral model in Figure 1, and the nature of the hydrogen bonding is depicted in Figure A1. Selected interatomic distances and angles as well as bond valence sums are summarized in Tables A8–A10.

Table A6. Final results from neutron refinement of akdalaite ($\text{Al}_{10}\text{O}_{14}(\text{OH})_2$).

Site	Wyck Pos.	<i>x</i>	<i>y</i>	<i>z</i>	$U_{\text{iso}} (\times 10^2) \text{ \AA}^2$
Al1	6c	0.8341(2)	0.6683(4)	0.9785(3)	0.51
Al2	2b	1/3	2/3	0.7690(7)	0.94
Al3	2b	1/3	2/3	0.160945)	0.59
O1	2a	0	0	0.0970(4)	0.51
O2	6c	0.9728(2)	0.4864(1)	0.1143(3)	0.59
O3	6c	0.1646(3)	0.8354(3)	0.8745(3)	0.64
O4 *	2b	2/3	1/3	0.8682	0.55
H1 **	6c	0.0423(12)	0.0212(6)	0.2134(7)	1.5(1)

* *z* positional parameter not refined in order to fix the unit cell origin; ** Occupancy of H site fixed at $1/3$ after moving from ideal position $2a$ (symmetry, $3m$; multiplicity, $M = 2$) to $6c$ (m ; $M = 6$).

Unit cell: hexagonal, $P6_3mc$; $a = 5.57610(2) \text{ \AA}$, $c = 8.77247(6) \text{ \AA}$; Volume = $236.068(3) \text{ \AA}^3$.

Refinement statistics: $R_{\text{wp}} = 3.77\%$ GOF = 1.82 for neutron data (6541 observations); the integrated Bragg discrepancy factor, $R_B(F^2)$, was 5.30%.

Table A7. Refined akdalaite anisotropic displacement parameters from NPD data ($\text{Å}^2 \times 10^2$).

Site	U_{11}	U_{12}	U_{13}	U_{22}	U_{23}	U_{33}
Al1	0.35(3)	0.20(2)	0.17(2)	0.40(5)	0.33(5)	0.78(6)
Al2	1.03(8)	0.51(4)	0	1.03(8)	0.0	0.8(1)
Al3	0.39(4)	0.20(2)	0	0.39(4)	0	1.0(1)
O1	0.47(4)	0.24(2)	0	0.47(4)	0	0.57(8)
O2	0.47(3)	0.24(1)	−0.14(4)	0.50(2)	−0.07(2)	0.77(4)
O3	0.59(3)	0.37(5)	0.21(2)	0.59(4)	−0.21(2)	0.84(4)
O4	0.60(5)	0.30(3)	0.0	0.60(5)	0	0.5(1)
H1 *	Uiso = 1.5(1)					

* The H1 site was refined isotropically.

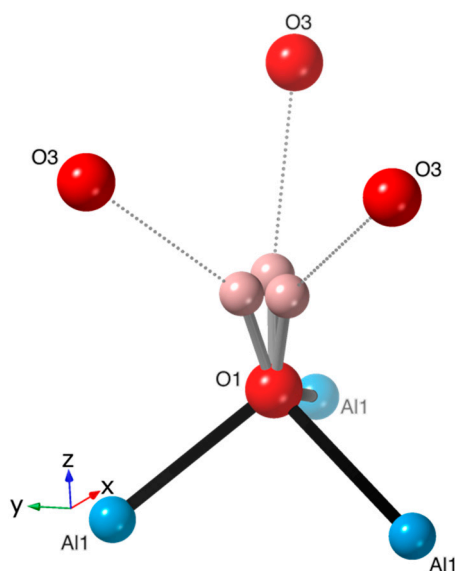
**Figure A1.** Bonding environment around the threefold split site for H1 showing bonding to O1 and H-bonding (dotted line) to O3 at distances of 1.075(7) and 1.990(8) Å , respectively.

Table A8. Selected interatomic distances (Å) and angles (°) for akdalaite (Al₁₀O₁₄(OH)₂) from analysis of NPD data.

Al11	To	Dist.	$s_{ij}/\Sigma s_{ij}$ *	O2	O2	O3	O3	O4
	O1	1.910(2)	0.50	92.59(9)	92.60(9)	84.36(9)	84.37(9)	177.9(1)
	O2	1.957(1)	0.44	81.73(8)	90.53(7)	171.6(1)	85.84(8)	
	O2	1.957(1)	0.44	171.6(1)	90.55(7)	85.85(8)		
	O3	1.838(1)	0.60	97.0(1)	96.98(8)			
	O3	1.838(1)	0.60	97.00(8)				
	O4	1.885(2)	0.53					
BVS								
Al1			3.11					
Al2	To	dist.		O2	O2	O3	O3	O3
	O2	2.007(3)	0.38	79.3(1)	79.3(1)	90.78(6)	167.0(2)	90.78(6)
	O2	2.007(3)	0.38	79.3(1)	90.78(6)	90.78(6)	167.0(2)	
	O2	2.007(3)	0.38	167.0(2)	90.78(6)	90.77(6)		
	O3	1.874(3)	0.55	97.7(2)	97.7(2)			
	O3	1.874(3)	0.55	97.7(2)				
	O3	1.874(3)	0.55					
BVS								
Al2			2.79					
Al3	To	dist.		O2	O2	O4		
	O2	1.788(1)	0.69	114.93(7)	114.96(7)	103.2(1)		
	O2	1.789(1)	0.69	114.93(7)	103.2(1)			
	O2	1.788(1)	0.69	103.2(1)				
	O4	1.818(4)	0.64					
BVS								
Al3			2.71					
H1	To	Dist.		O3				
	O1	1.042(7)	0.60	146.9(3)				
	O3	1.979(7)	0.22					
BVS H1			0.83					

* Bond valence $s_{ij} = \exp((R_0 - R_{ij})/B)$, where R_{ij} is the length of a bond between atoms i and j ; Σs_{ij} , the BVS around each atom should be equal to the valence (oxidation state) of that atom. For the values quoted, the parameters R_0 and B were taken from tabulations provided at the International Union of Crystallography: <https://www.iucr.org/resources/data/datasets/bond-valence-parameters> [39]. The R_0 and B parameters used were those compiled for Al³⁺ (1.651, 0.37) and H¹⁺ (0.569, 0.94) bonded to O²⁻.

Table A9. Akdalaite oxygen bond valence sums with hydrogen contribution.

Site	BVS	Type
O1	2.10	O-H
O2	1.95	
O3	2.00	O...H
O4	2.15	

Table A10. Metal–metal distances in akdalaite and the Michel model (MM) of ferrihydrite [9].

Atom Pair	Type	d (Å)	
		Akdalaite (M = Al)	MM-Ferrihydrite (M = Fe)
M1 – M1	Edge	2.802	2.907
M1 – M2	Edge	3.018	3.261
M1 – M2	Corner	3.339	3.409

References

1. Alivisatos, A.P.; Barbara, P.F.; Castleman, A.W.; Chang, J.; Dixon, D.A.; Klein, M.L.; McLendon, G.L.; Miller, J.S.; Ratner, M.A.; Rossky, P.J.; et al. From molecules to materials: Current trends and future directions. *Adv. Mater.* **1998**, *10*, 1297–1336. [[CrossRef](#)]

2. Hochella, M.F.; Lower, S.K.; Maurice, P.A.; Penn, R.L.; Sahai, N.; Sparks, D.L.; Twining, B.S. Nanominerals, mineral nanoparticles, and Earth systems. *Science* **2008**, *319*, 1631–1635. [[CrossRef](#)]
3. Banfield, J.F.; Zhang, H.Z. Nanoparticles in the environment. *Rev. Mineral. Geochem.* **2001**, *44*, 1–58. [[CrossRef](#)]
4. Paterson, G.; Macken, A.; Thomas, K.V. The need for standardized methods and environmental monitoring programs for anthropogenic nanoparticles. *Anal. Methods* **2011**, *3*, 1461–1467. [[CrossRef](#)]
5. Sadik, O.A. Anthropogenic nanoparticles in the environment. *Environ. Sci. Process. Impacts* **2013**, *15*, 19–20. [[CrossRef](#)]
6. Schwertmann, U.; Cornell, R.M. *Iron Oxides in the Laboratory: Preparation and Characterization*, 2nd ed.; Wiley-VCH: Weinheim, Germany, 2000; p. 188.
7. Sangaiya, P.; Jayaprakash, R. A Review on Iron Oxide Nanoparticles and Their Biomedical Applications. *J. Supercond. Nov. Magn.* **2018**, *31*, 3397–3413. [[CrossRef](#)]
8. Pouran, S.R.; Raman, A.A.A.; Daud, W. Review on the application of modified iron oxides as heterogeneous catalysts in Fenton reactions. *J. Clean. Prod.* **2014**, *64*, 24–35. [[CrossRef](#)]
9. Michel, F.M.; Barron, V.; Torrent, J.; Morales, M.P.; Serna, C.J.; Boily, J.F.; Liu, Q.S.; Ambrosini, A.; Cismasu, A.C.; Brown, G.E. Ordered ferrimagnetic form of ferrihydrite reveals links among structure, composition, and magnetism. *Proc. Natl. Acad. Sci. USA* **2010**, *107*, 2787–2792. [[CrossRef](#)] [[PubMed](#)]
10. Michel, F.M.; Ehm, L.; Antao, S.M.; Lee, P.; Chupas, P.J.; Liu, G.; Strongin, D.R.; Schoonen, M.A.A.; Phillips, B.L.; Parise, J.B. The Structure of Ferrihydrite, a Nanocrystalline Material. *Science* **2007**, *316*, 1726–1729. [[CrossRef](#)]
11. Parise, J.B.; Ehm, L.; Michel, F.M.; Antao, S.; Chupas, P.J.; Lee, P.L.; Martin, C.D.; Shastri, S. Towards a better understanding of the structure of nano-minerals at ambient and extreme conditions. In *Synchrotron Radiation in Materials Science*; Paniago, R.M., Ed.; Wiley: London, UK, 2009; Volume 1092, pp. 41–44.
12. Casey, W.H.; Phillips, B.L.; Furrer, G. Aqueous aluminum polynuclear complexes and nanoclusters: A review. *Rev. Mineral. Geochem.* **2001**, *44*, 167–190. [[CrossRef](#)]
13. Jensen, K.M.O.; Andersen, H.L.; Tyrsted, C.; Bojesen, E.D.; Dippel, A.C.; Lock, N.; Billinge, S.J.L.; Iversen, B.B.; Christensen, M. Mechanisms for Iron Oxide Formation under Hydrothermal Conditions: An in Situ Total Scattering Study. *ACS Nano* **2014**, *8*, 10704–10714. [[CrossRef](#)] [[PubMed](#)]
14. Sadeghi, O.; Zakharov, L.N.; Nyman, M. Aqueous formation and manipulation of the iron-oxo Keggin ion. *Science* **2015**, *347*, 1359–1362. [[CrossRef](#)] [[PubMed](#)]
15. Wefers, K.; Misra, C. *Oxides and Hydroxides of Aluminum*; Alcoa Technical Paper No. 19, Revised; Alcoa Laboratories, 1987; Available online: http://epsc511.wustl.edu/Aluminum_Oxides_Alcoa1987.pdf (accessed on 11 May 2019).
16. Weatherill, J.S.; Morris, K.; Bots, P.; Stawski, T.M.; Janssen, A.; Abrahamsen, L.; Blackham, R.; Shaw, S. Ferrihydrite Formation: The Role of Fe-13 Keggin Clusters. *Environ. Sci. Technol.* **2016**, *50*, 9333–9342. [[CrossRef](#)] [[PubMed](#)]
17. Jambor, J.L.; Dutrizac, J.E. Occurrence and constitution of natural and synthetic ferrihydrite, a widespread iron oxyhydroxide. *Chem. Rev.* **1998**, *98*, 2549–2585. [[CrossRef](#)] [[PubMed](#)]
18. Drits, V.A.; Sakharov, B.A.; Salyn, A.L.; Manceau, A. Structural Model for Ferrihydrite. *Clay Miner.* **1993**, *28*, 185–207. [[CrossRef](#)]
19. Manceau, A. Evaluation of the structural model for ferrihydrite derived from real-space modelling of high-energy X-ray diffraction data. *Clay Miner.* **2009**, *44*, 19–34. [[CrossRef](#)]
20. Manceau, A. PDF analysis of ferrihydrite and the violation of Pauling’s Principia. *Clay Miner.* **2010**, *45*, 225–228. [[CrossRef](#)]
21. Manceau, A. Critical evaluation of the revised akdalaite model for ferrihydrite. *Am. Mineral.* **2011**, *96*, 521–533. [[CrossRef](#)]
22. Manceau, A.; Skanthakumar, S.; Soderholm, L. PDF analysis of ferrihydrite: Critical assessment of the under-constrained akdalaite model. *Am. Mineral.* **2014**, *99*, 102–108. [[CrossRef](#)]
23. Sterner, S.M. Precise Pressure Control in Hydrothermal Experiments with Cold-Seal Pressure-Vessels. *Am. Mineral.* **1994**, *79*, 1150–1152.
24. Rosenberg, P.E. Stability relations of aluminum hydroxy-fluoride hydrate, a ralstonite-like mineral, in the system $AlF_3-Al_2O_3-H_2O-HF$. *Can. Mineral.* **2006**, *44*, 125–134. [[CrossRef](#)]

25. Furrer, G.; Phillips, B.L.; Ulrich, K.U.; Pothig, R.; Casey, W.H. The origin of aluminum floes in polluted streams. *Science* **2002**, *297*, 2245–2247. [[CrossRef](#)] [[PubMed](#)]
26. Agilent. *CrysAlis PRO*; Agilent Technologies Ltd.: Oxfordshire, UK, 2014.
27. Palatinus, L.; Chapuis, G. Superflip—A computer program for the solution of crystal structures by charge flipping in arbitrary dimensions. *J. Appl. Crystallogr.* **2007**, *40*, 786–790. [[CrossRef](#)]
28. Petricek, V.; Dusek, M.; Palatinus, L. Crystallographic Computing System JANA2006: General features. *Z. Krist.-Cryst. Mater.* **2014**, *229*, 345–352.
29. Sheldrick, G.M. A short history of SHELX. *Acta Crystallogr A* **2008**, *64*, 112–122. [[CrossRef](#)] [[PubMed](#)]
30. Yamaguchi, G.; Okumiya, M. Refinement of structure of tohdite $5\text{Al}_2\text{O}_3 \cdot \text{H}_2\text{O}$. *B Chem. Soc. Jpn.* **1969**, *42*, 2247–2249. [[CrossRef](#)]
31. Larson, A.C.; von Dreele, R.B. *General Structure Analysis System (GSAS)*; Report LAUR 86-748; Los Alamos National Laboratory: Los Alamos, New Mexico, 2000.
32. Toby, B.H. EXPGUI, a graphical user interface for GSAS. *J. Appl. Crystallogr.* **2001**, *34*, 210–213. [[CrossRef](#)]
33. Parise, J.B.; Leinenweber, K.; Weidner, D.J.; Tan, K.; Vondreele, R.B. Pressure-Induced H-Bonding—Neutron Diffraction Study of Brucite, $\text{Mg}(\text{OD})_2$, to 9.3 Gpa. *Am. Mineral.* **1994**, *79*, 193–196.
34. Parise, J.B.; Theroux, B.; Li, R.; Loveday, J.S.; Marshall, W.G.; Klotz, S. Pressure dependence of hydrogen bonding in metal deuterioxides: A neutron powder diffraction study of $\text{Mn}(\text{OD})_2$ and $\beta\text{-Co}(\text{OD})_2$. *Phys. Chem. Miner.* **1998**, *25*, 130–137. [[CrossRef](#)]
35. Xue, X.Y.; Kanzaki, M. Proton Distributions and Hydrogen Bonding in Crystalline and Glassy Hydrous Silicates and Related Inorganic Materials: Insights from High-Resolution Solid-State Nuclear Magnetic Resonance Spectroscopy. *J. Am. Ceram. Soc.* **2009**, *92*, 2803–2830. [[CrossRef](#)]
36. Yesinowski, J.P.; Eckert, H.; Rossman, G.R. Characterization of Hydrous Species in Minerals by High-Speed H-1 Mas Nmr. *J. Am. Chem. Soc.* **1988**, *110*, 1367–1375. [[CrossRef](#)]
37. Brown, I.D.; Altermatt, D. Bond-Valence Parameters Obtained from a Systematic Analysis of the Inorganic Crystal-Structure Database. *Acta Crystallogr. B* **1985**, *41*, 244–247. [[CrossRef](#)]
38. Brown, I.D. Recent Developments in the Methods and Applications of the Bond Valence Model. *Chem. Rev.* **2009**, *109*, 6858–6919. [[CrossRef](#)]
39. Brown, I.D. *The chemical Bond in Inorganic Chemistry: The Bond Valence Model*; Oxford University Press: Oxford, UK; New York, NY, USA, 2002; 278p.
40. Yu, D.Q.; Xue, D.F.; Ratajczak, H. Golden ratio and bond-valence parameters of hydrogen bonds of hydrated borates. *J. Mol. Struct.* **2006**, *783*, 210–214. [[CrossRef](#)]
41. Maslen, E.N.; Streltsov, V.A.; Streltsova, N.R.; Ishizawa, N. Synchrotron X-Ray Study of the Electron-Density in $\alpha\text{-Fe}_2\text{O}_3$. *Acta Crystallogr B* **1994**, *50*, 435–441. [[CrossRef](#)]
42. Pauling, L. The principles determining the structure of complex ionic crystals. *J. Am. Chem Soc.* **1929**, *51*, 1010–1026. [[CrossRef](#)]
43. Page, K.; Hood, T.C.; Proffen, T.; Neder, R.B. Building and refining complete nanoparticle structures with total scattering data. *J. Appl. Crystallogr.* **2011**, *44*, 327–336. [[CrossRef](#)]
44. Harrington, R.; Neder, R.B.; Parise, J.B. The nature of X-ray scattering from geo-nanoparticles: Practical considerations of the use of the Debye equation and the pair distribution function for structure analysis. *Chem. Geol.* **2011**, *329*, 3–9. [[CrossRef](#)]
45. Parise, J.B.; Woerner, W.R.; Neder, R.B. Synchrotron powder diffraction methods and refinement techniques. In *CMS Workshop Lecture Series Volume 19: Advanced Applications of Synchrotron Radiation in Clay Science*; Waychunas, G.A., Ed.; Clay Minerals Society: Chantilly, VA, USA, 2014; Volume 19, pp. 33–68.
46. Hiemstra, T. Surface and mineral structure of ferrihydrite. *Geochim. Cosmochim. Acta* **2013**, *105*, 316–325. [[CrossRef](#)]

